ELSEVIER

Contents lists available at ScienceDirect

# Chemical Engineering Journal

journal homepage: www.elsevier.com/locate/cej





# Single-step synthesis of oxygen-doped hollow porous graphitic carbon nitride for photocatalytic ciprofloxacin decomposition

Chitiphon Chuaicham <sup>a</sup>, Karthikeyan Sekar <sup>a,e</sup>, Yihuang Xiong <sup>b</sup>, Vellaichamy Balakumar <sup>a</sup>, Yanisa Mittraphab <sup>c</sup>, Kuniyoshi Shimizu <sup>c</sup>, Bunsho Ohtani <sup>d</sup>, Ismaila Dabo <sup>b</sup>, Keiko Sasaki <sup>a,d,\*</sup>

- <sup>a</sup> Department of Earth Resources Engineering, Kyushu University, Fukuoka 819-0395, Japan
- b Department of Materials Science and Engineering, The Pennsylvania State University, University Park, PA 16802, United States
- Faculty of Agriculture, Kyushu University, Fukuoka 812-8581, Japan
- <sup>d</sup> Institute for Catalysis, Hokkaido University, Sapporo 001-0021, Japan
- e Department of Chemistry, Faculty of Engineering and Technology, SRM Institute of Science and Technology, Kattankulathur, Tamil Nadu 603203, India

#### ARTICLE INFO

# Keywords: Photocatalyst Ciprofloxacin degradation Oxygen-doped carbon nitride Porous hollow graphitic carbon nitride

#### ABSTRACT

Pollutants degradation via visible-light driven photocatalysts have attracted interest as a potentially efficient and sustainable approach for wastewater treatment. In the present study, a series of oxygen-doped hollow porous surface graphitic carbon nitride (OCN) has been prepared by one-pot thermal polycondensation of melamine with different amounts of polyoxyethylene stearyl ether as the oxygen source and template. The prepared OCN samples were utilized for the photocatalytic ciprofloxacin (CIP) degradation, which is a pharmaceutical waste, under visible light irradiation. The highest degradation performance for CIP was obtained from the OCN sample with 1 mg polyoxyethylene stearyl, which was three times greater than that of pristine C<sub>3</sub>N<sub>4</sub>. The superior degradation performance of the OCN samples were observed due to the improved light absorption, less recombination rate of photogenerated electron and hole, and enhanced electron transportation, which was proven through the PL, photocurrent density, and EIS results. Thus, the proposed one-pot synthesis of OCN provides an effective method in producing potential photocatalysts for the removal of organic pollutants, such as discarded pharmaceuticals, in wastewater.

## 1. Introduction

Photocatalysis is a conceptually simple and environmentally sustainable alternative to the degradation of hazardous chemicals at trace concentrations using solar irradiation [1–4]. There are many photocatalysts used for water and gas treatment.; Huang et al reported the efficient degradation of organic dye (rhodamine B) using cubic Cu<sub>2</sub>O nanoparticles wrapped by reduced graphene oxide [5]. The efficient photocatalytic removal of nitric oxide was reported using CuInZnS nanoporous structures [6] and  $MoS_2/g$ -C<sub>3</sub>N<sub>4</sub> nanocomposites [7]. In the field of photocatalysis for pollution treatment, graphitic carbon nitride (C<sub>3</sub>N<sub>4</sub>) has attracted significant attention because of its abundance and excellent visible-light activity [8–11]. However, the practical applications of pristine C<sub>3</sub>N<sub>4</sub> are limited due to its low conductivity, specific active surface, and light harvesting ability, as well as its inefficient separation of photogenerated charge carriers [12]. Various strategies, such as nanostructure design, element doping, pore generation, and

heterostructure construction, have been adopted to improve the photoactivity of pristine C<sub>3</sub>N<sub>4</sub> [13-18]. Among these, increasing the porosity and non-metal elemental doping have resulted in excellent photocatalytic activity by providing a narrow band gap, porous structure, and large specific surface area (SSA). For example, the incorporation of heteroatoms, such as N, B, P, S, O, and Cl, can significantly improve the electronic properties of C<sub>3</sub>N<sub>4</sub>, reduce recombination, and enhance visible light compatibility and photocatalytic activity [14,19-23]. Liu et al. [24] reported the excellent photocatalytic performance of porous C<sub>3</sub>N<sub>4</sub> toward sulfamethoxazole. Guo et al. [25] found that tetracycline degradation under visible light using Cl-doped porous C<sub>3</sub>N<sub>4</sub> nanosheets promoted electron transfer and inhibited recombination. Fu et al. [26] noted that doping hierarchically porous C<sub>3</sub>N<sub>4</sub> tubes with O significantly enhanced photocatalytic CO<sub>2</sub> reduction compared to other heteroatoms. In addition, Wei et al. [27] reported that O self-doped C<sub>3</sub>N<sub>4</sub> with a narrow band gap resulted in enhanced photocatalytic performance compared to pristine C<sub>3</sub>N<sub>4</sub>.

E-mail address: keikos@mine.kyushu-u.ac.jp (K. Sasaki).

<sup>\*</sup> Corresponding author.

Recently, there has been increasing interest in the study of hollow  $C_3N_4$  structures owing to their improved visible light harvesting through multiple reflections of incident light within their interior voids [28–31]. Hollow structures have been prepared using silica templates, C spheres, and polymer latex [29,32,33]. Template removal is challenging through this method due to the harsh conditions and environmentally harmful nature of the process. Shi et al. [34] reported spherical mesoporous  $C_3N_4$  with a large surface area that exhibits high photoactivity. Sun et al. [35] synthesized hollow semiconductor  $C_3N_4$  nanospheres using a bioinspired method, resulting in enhanced photocatalytic activity. However, these studies used environmentally harmful and toxic hydrofluoric acid to remove the templates. Therefore, a simple, cost effective, and environmentally friendly template removal method is necessary to obtain a porous  $C_3N_4$  structure with a hollow morphology which is feasible for large-scale production.

The present protocol consists of synthesizing hollow porous  $C_3N_4$  structures through an in-situ thermal polycondensation method using polyoxyethylene stearyl ether as the template; the chemical structure is shown in Fig. S1a. This strategy simultaneously formed the O-doped hollow porous  $C_3N_4$  (hereafter, OCN) surface and removed the template. The materials were characterized using ultraviolet differential reflectance spectroscopy (UV-DRS), X-ray photoelectron spectroscopy (XPS), the Brunauer–Emmett–Teller (BET) method, scanning electron microscopy (SEM), transmission electron microscopy (TEM), and mapping analysis. The photocatalytic charge separation and electron transfer mechanism were investigated through DRS and theoretical calculations. This study delivers a simple and environmentally friendly approach for the fabrication of multifunctional  $C_3N_4$  with excellent photocatalytic activity and reusability.

# 2. Materials and methods

#### 2.1. Materials and reagents

Melamine, polyoxyethylene (20) stearyl ether, p-benzoquinone (BQ), acetonitrile, isopropanol (IPA), and ethylenediaminetetraacetic acid disodium (EDTA-2Na) were obtained from Fujifilm Wako Pure Chemical Co. (Osaka, Japan). CIP was purchased from Fumakoshi Co., Tokyo, Japan.

# 2.2. Synthesis of CN and OCN

OCN samples were prepared from melamine and polyoxyethylene stearyl ether through thermal polycondensation. First, 1 g of melamine was mixed with various amounts of polyoxyethylene stearyl ether (0.5, 1, and 5 mg) by grinding in a mortar. The mixed solid was transferred into a crucible and calcinated at 500  $^{\circ}$ C for 2 h under ambient conditions. The obtained products were denoted as OCN-0.5, OCN-1, and OCN-5, where the numbers refer to the weight of polyoxyethylene stearyl ether in mg. CN was prepared by the same process without the addition of polyoxyethylene stearyl ether.

# 2.3. Characterizations

An Ultima IV diffractometer (RIGAKU, Akishima, Japan) was used to measure X-ray diffraction (XRD) patterns of the samples (scanning speed =  $2^{\circ}$ /min, scan step size =  $0.02^{\circ}$ ). Fourier-transform infrared (FTIR) spectroscopy (Jasco FTIR-670 Plus (Tokyo, Japan)) was used to confirm the functional groups of the composite materials. The BET-SSA was characterized using the N adsorption—desorption isotherm with a BELSORP max porosimeter. Surface structure and morphology of the prepared samples were confirmed by SEM and TEM using a VE-9800 SEM and JEM-2100HCKM, respectively. The visible-light absorbance properties of the samples were identified by UV–Vis/DRS (Shimadzu UV-2450). The chemical composition of the samples was measured by XPS (ESCA 5800; ULVAC-PHI, Inc., Kanagawa, Japan). C, H, and N

(CHN) concentrations were measured by a Yanaco CHN Corder MT-5. Photoluminescence (PL) spectroscopy was conducted using an FP-6600 spectrofluorometer. Energy-resolved distribution of electron trap (ERDT) patterns of the prepared materials were found by reversed double-beam photoacoustic spectroscopy (RDB-PAS) from 650 to 350 nm using an amplifier to multiply the photoacoustic signals. The degradation products were identified by mass spectrometry (UPLC/qTOF-MS). The total organic carbon (TOC) content was examined using a TOC analyzer (TOC-V CHS, Shimazu, Japan). The concentration of fluoride ions released after photocatalytic CIP degradation was investigated by ion chromatography (IC, ICS-2100, Thermo Scientific, Waltham, US).

# 2.4. Photocatalytic test

The CIP degradation performance of the samples was evaluated under visible light (500 W Xe lamp with a UV cut-off filter, > 380 nm, Fig. S1b). 50 mg of the prepared materials were added to 50 mL 10 ppm CIP solution. The solution achieved adsorption-desorption equilibrium after 30 min under dark conditions. The solution was then irradiated from above while being stirred. An external cooling jacket maintained a reaction temperature of 25 °C. At the time interval, 1.0 mL of solution was removed to examine the remaining CIP concentration by highperformance liquid chromatography with a C18 column. A mixture of 20% 5 mM CH<sub>3</sub>COONa, 15% acetonitrile, and 65% 2% v/v acetic acid was used as the mobile phase. Finally, we confirmed the active species  $(O_2^-, \cdot OH, \text{ and } h^+)$  through a scavenger tests. In this experiment, 2–50 mM (0.1 mmol- 2.5 mmol) of IPA, BQ, and EDTA-2Na were used as the hydroxyl radical, superoxide radical, and hole scavengers, respectively. Moreover, the binary system of scavenger by mixing of two scavengers such as 10 mM of IPA with 10 mM of BQ, 10 mM of IPA with 10 mM of EDTA-2Na and 10 mM of BQ with 10 mM of EDTA-2Na were performed and compared with the single scavenger (IPA, BQ, and EDTA-2Na alone) system to clarify the role of each active species,  $O_2^-$ , •OH, and  $h^+$ .

# 2.5. Density functional theory (DFT) calculations

Vienna Ab-initio Simulation Package software was used for the DFT calculations [36]. The effective (Kohn-Sham) electronic potential was described at the Perdew-Burke-Ernzerhof (PBE) semilocal level [37]. We employed the Grimme-D2 method to describe the van der Waals interactions [38]. Pristine monolayer  $C_3N_4$  was simulated using a  $2 \times 2$ × 1 supercell containing 56 atoms. A vacuum separation of 15 Å was inserted between the periodic images orthogonal to the layers. Structural optimization was carried out with a plane-wave cutoff of 520 eV and the Brillouin zone was sampled with a  $2 \times 2 \times 1$   $\Gamma$ -centered Monkhorst-Pack grid [39]. The total energy and forces were converged within less than  $10^{-6}$  eV and 0.01 eV/Å, respectively. The preferential doping sites in CN were previously investigated [40], suggesting N<sub>edge</sub> substitution is energetically favorable. Thus, we constructed OCN by substituting one N atom with an O atom in the supercell. The band structure and projected density of states (PDOS) of the CN and OCN samples were calculated [41]. The hybrid Heyd-Scuseria-Ernzerhof functional [42] with 25% exact exchange was employed to mitigate the underestimation of the band gap within semilocal PBE approximations.

# 2.6. Bio-toxicity test of CIP and photodegraded CIP solution

To examine the bio-toxicity of the solution after photocatalytic treatment, the growth of *Escherichia coli* ( $E.\ coli$ ) as test bacterium in the presence of CIP and degraded CIP solution was evaluated. In the experiment, the  $E.\ coli$  was subcultured on a Difco<sup>TM</sup> nutrient agar (BD Biosciences) and incubated overnight at 37 °C.  $E.\ coli$  colonies were then needled into 10 mL of nutrient broth and incubated for 24 h at 37 °C. The density of the bacteria suspensions was adjusted to  $10^5$  colony forming units (cfu)/mL, and this value was confirmed using a UV–visible/near-IR

spectrophotometer at 630 nm. The bacteria suspensions were diluted to  $10^3\,$  cfu/mL for testing. For the bio-toxicity experiment, the diluted bacteria solution was mixed with the CIP or degraded CIP solution in 1:1 v/v. 1 mL of the mixing solution was dispersed on the surface of an MC-media pad (JNC Corporation), which was used as a plate to grow the *E. coli*, followed by incubation at 37 °C for 24 h. Blue areas indicate the growth and survival of the *E. coli*; these areas will have had little anti-bacterial activity, which implies that the presence of these solutions in wastewater is relatively safe.

# 3. Results and discussion

#### 3.1. XRD results

The crystallographic and phase structure of the CN and OCN materials were investigated by XRD analysis, as shown in Fig. 1a. All samples exhibit characteristic  $\rm C_3N_4$  diffraction peaks at approximately 12.9° and 27.6°, corresponding to the (100) and (002) planes, which can be assigned to the interlayer distance d of 0.33 nm and the in-plane structural packing of 0.675 nm, respectively. These diffraction peaks are in good agreement with the  $\rm C_3N_4$  phase (JCPDS no. 87–1526). The appearance of these peaks confirms the successful doping of O in the CN structure with no impurity phase observed. Meanwhile, the lower intensity peak of the (002) plane in the OCN samples can be ascribed to the decreased layered morphology in the porous microstructure. OCN-5 demonstrated the lowest (002) peak intensity, indicating the highest porosity.

#### 3.2. FT-IR results

The functional groups of the prepared CN and OCN were examined by FT-IR spectroscopy. Fig. 1b presents the FTIR spectra of the samples. There are no significant differences in the FTIR spectra of the OCN and CN samples. The bands observed from 1200 to 1650 cm $^{-1}$  correspond to the stretching mode of CN heterocycles. The peaks centered at 1641, 1570, and 1414 cm $^{-1}$  are assigned to heptazine ring stretching. The absorption bands at 1324 and 1243 cm $^{-1}$  correspond to heptazine bending. The representative peak at 883 cm $^{-1}$  is ascribed to the N–H deformation mode. The peak at 810 cm $^{-1}$  is a characteristic of the tri-3 striazine breathing mode. The broad bands in the 2900–3500 cm $^{-1}$  range are ascribed to the N–H vibration of  $\rm C_3N_4$  and surface-adsorbed H<sub>2</sub>O. The additional weak peak at 2377 cm $^{-1}$  corresponds to the physically adsorbed CO<sub>2</sub> on the C<sub>3</sub>N<sub>4</sub> surface. Peaks attributed to C–O–C stretching are not observed in the OCN samples due to the low O concentration.

## 3.3. Optical properties

The optical properties, including the light-harvesting nature and energy band gap of the photocatalyst, were examined by UV-DRS analysis. In Fig. 2a, the CN and OCN samples exhibit an absorption edge at approximately 470 nm. As the amount of polymer precursor used increased, the light absorption behavior of the samples increased significantly and broadened in the visible light (i.e., higher wavelength) region. The light absorbance of the OCN samples is significantly higher than that of the CN sample, suggesting the effectivity of OCN in producing and separating electrons during the photocatalytic reaction.

The band gap energy,  $E_g$ , of the CN and OCN samples were found by transforming the results obtained from UV-DRS using Tauc's equation.

$$(\alpha h \nu)^{1/2} = A(h \nu - E_g), \tag{1}$$

where  $\alpha$ , h,  $\nu$ , and A are the absorption coefficient, Planck constant, frequency of observed light, and proportionality constant, respectively [43–45]. The band gap energies estimated using  $(\alpha h \nu)^2$  were plotted against the of the light energy, resulting in the  $E_g$  plot shown in Fig. 2b. The  $E_g$  values of CN, OCN-0.5, OCN-1, and OCN-5 were 2.82, 2.79, 2.77, and 2.73 eV, respectively, which are in good agreement with the UV-DRS results. For the OCN samples,  $E_g$  was observed to decrease. Hence, the lower  $E_g$  and higher visible light absorption of the OCN samples could produce more hot carriers with higher efficiency than CN.

## 3.4. BET and average pore diameter results

The isotherms of  $\rm N_2$  adsorption–desorption and distribution of pore size for all materials were determined, as shown in Fig. 3a. The materials display a type-IV isotherm (H3-type hysteresis loops), implying their porous microstructure. From the BET analysis, the SSAs of CN, OCN-0.5, OCN-1, and OCN-5 are 5.1, 10.4, 18.2, and 22.7 m²/g, respectively. This indicates that the SSA of the OCN samples is at least twice that of pure CN because gas production during the thermal polycondensation of melamine with polyoxyethylene stearyl ether can generate porous  $\rm C_3N_4$ . The average pore diameter size of the CN and OCN samples was fitted using the Barrett–Joyner–Halenda (BJH) model. From Fig. 3b, the OCN samples have average pore diameters of approximately 10–12 nm, indicating their highly porous structure.

# 3.5. XPS results

The elemental composition and surface molar ratio of the samples were examined. The survey scans (Fig. 4a) show that the primary elements in all samples are C and N. The CN sample has a low O content, which increases significantly with O doping. In the XPS C 1 s spectrum,

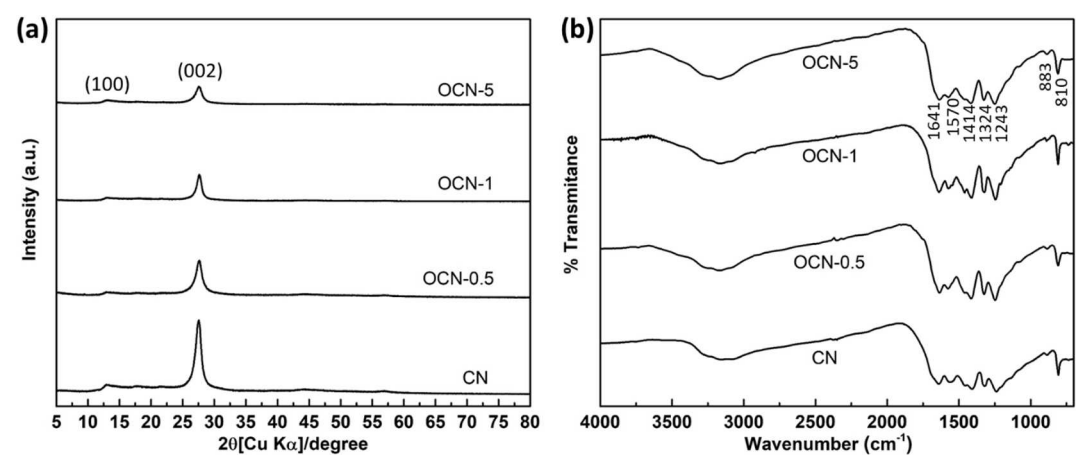


Fig. 1. (a) PXRD patterns and (b) FT-IR spectra of CN, OCN-0.5, OCN-1, and OCN-5.

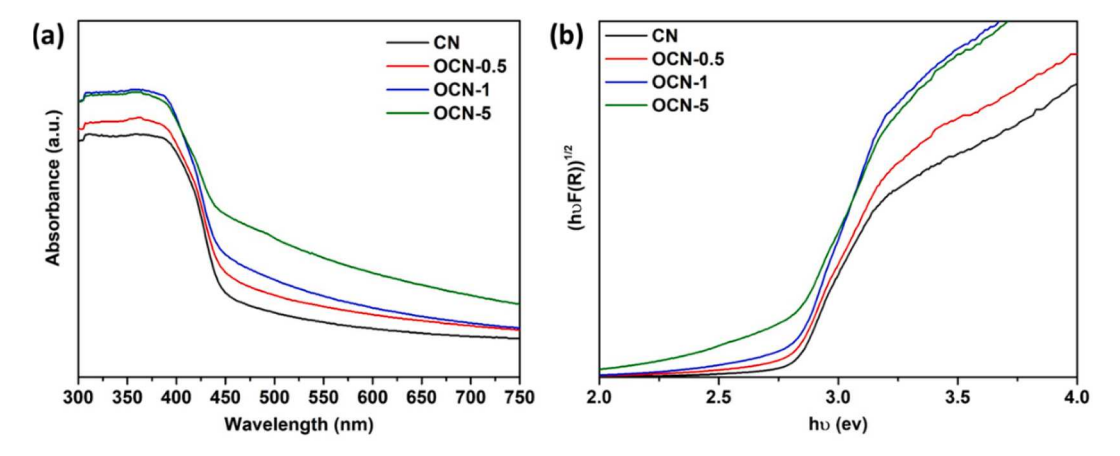


Fig. 2. (a) UV-vis DRS spectra and (b) energy band gap plots of CN, OCN-0.5, OCN-1, and OCN-5.

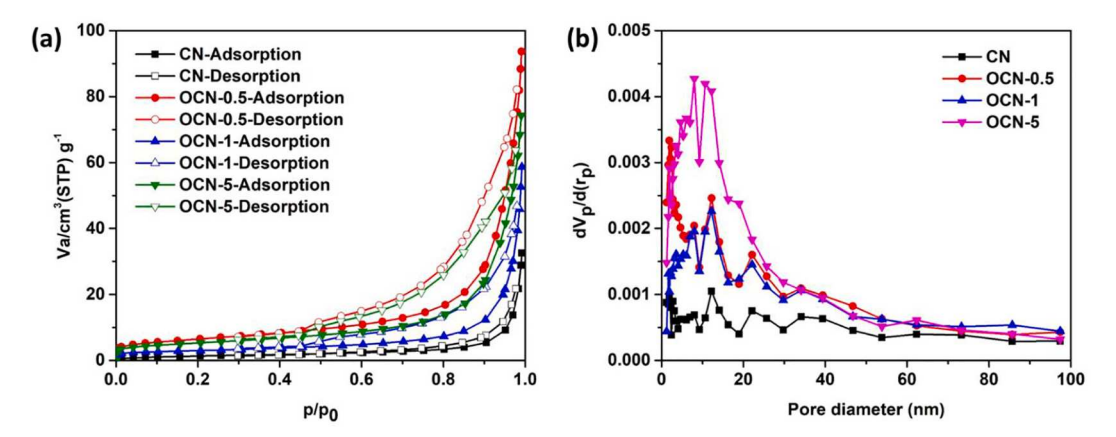


Fig. 3. (a) N<sub>2</sub> adsorption–desorption isotherms and (b) pore size distribution of CN, OCN-0.5, OCN-1, and OCN-5.

the C 1 s orbitals of the synthesized samples are deconvoluted as shown in Fig. 4b. Peaks are detected at 283.6 and 284.6 eV, corresponding to sp<sup>2</sup> (C–C) and sp<sup>3</sup> (C–C), respectively; these are due to C contamination in the instrument [46]. The peaks at 286.5 and 288.3 eV are assigned to the  $(C)_3$ -N and N-C = N bonds in the  $C_3N_4$  structure, respectively [47]. For the N 1 s spectra of the samples, as shown in Fig. 4c, three component peaks are noted at 398.8, 400.1, and 404.6 eV, ascribed to the C = N-C in the triazine ring, N-(C)<sub>3</sub> groups, and - NH<sub>2</sub> or = NH functional groups, respectively [40,48]. The O 1 s spectra of the samples exhibit two component peaks at approximately 532.3 and 534.1 eV, corresponding to the C = O bond and H<sub>2</sub>O, respectively, as shown in Fig. 4d [40]. Furthermore, the valence band (VB) of the materials was also investigated by XPS analysis. The estimated VBs of CN, OCN-0.5, OCN-1, and OCN-5 are 1.77, 1.69, 1.62, and 1.49 eV, respectively, as shown in Fig. 4e. The lowering of the VB after O doping is similar to that found in previous reports of O-doped C<sub>3</sub>N<sub>4</sub> [27].

From the UV-DRS results, the conduction bands (CBs) of CN, OCN-0.5, OCN-1, and OCN-5 are  $-1.05,\,-1.10,\,-1.15,\,$  and -1.24 eV, respectively. The surface molar ratio of O/N was explored using the relative sensitivity factors of O 1 s and N 1 s. For this calculation, the C–O bond peak of O 1 s was used to compare the excess O species in the backbone structure of  $C_3N_4$ . The O/N ratios of CN, OCN-0.5, OCN-1, and OCN-5 are 0.0075, 0.0601, 0.0751, and 0.0765, respectively, as shown in Fig. 4f. The surface molar ratio of O/N increases with the concentration of polyoxyethylene stearyl ether used, confirming the successful O doping of  $C_3N_4$ .

The C/N molar ratio of the samples was also examined using CHN analysis. The C/N ratios of CN, OCN-0.5, OCN-1, and OCN-5 are 0.6553, 0.6660, 0.6683, and 0.6694, respectively. The C/N molar ratio increases

with polyoxyethylene stearyl ether co-precursor concentration, suggesting that the excess O atoms in the OCN samples could be replaced with N atoms in the  $C_3N_4$  structure.

# 3.6. Morphology results

The surface structure of the CN and OCN samples were observed by SEM, as shown in Fig. 5. The CN and OCN samples have a distinct stacked structure. The CN sample has a smooth non-porous microstructure, while the OCN samples have a rough, porous microstructure. This suggests that the use of polyoxyethylene stearyl ether during  $C_3N_4$  synthesis can promote the porosity of  $C_3N_4$  due to the degradation of the polymer at high temperatures.

To further compare the detailed morphologies and crystal structures at high magnifications (50 and 200 nm), TEM observation was performed. From Fig. 6a and b, the morphology of the CN sample exhibits a sheet-like structure, similar to the SEM observation. On the other hand, OCN-1 possesses a hollow porous structure. The tubular structures of OCN-1 have a diameter of 9.6 nm. This indicates that the addition of polyoxyethylene stearyl ether induces the formation of a hollow porous  $C_3N_4$  structure with improved surface area and light absorption, thereby enhancing its photocatalytic activity. Elemental mapping with TEM-EDS analysis was also carried out for the OCN-1 sample to elucidate the location of the C, N, and O atoms in the structure. As shown in Fig. 6c, the EDS patterns of OCN-1 consist of C, N, and O. The locations of the O atoms overlap the C and N atoms, indicating the homogeneous distribution of O atoms in OCN-1.

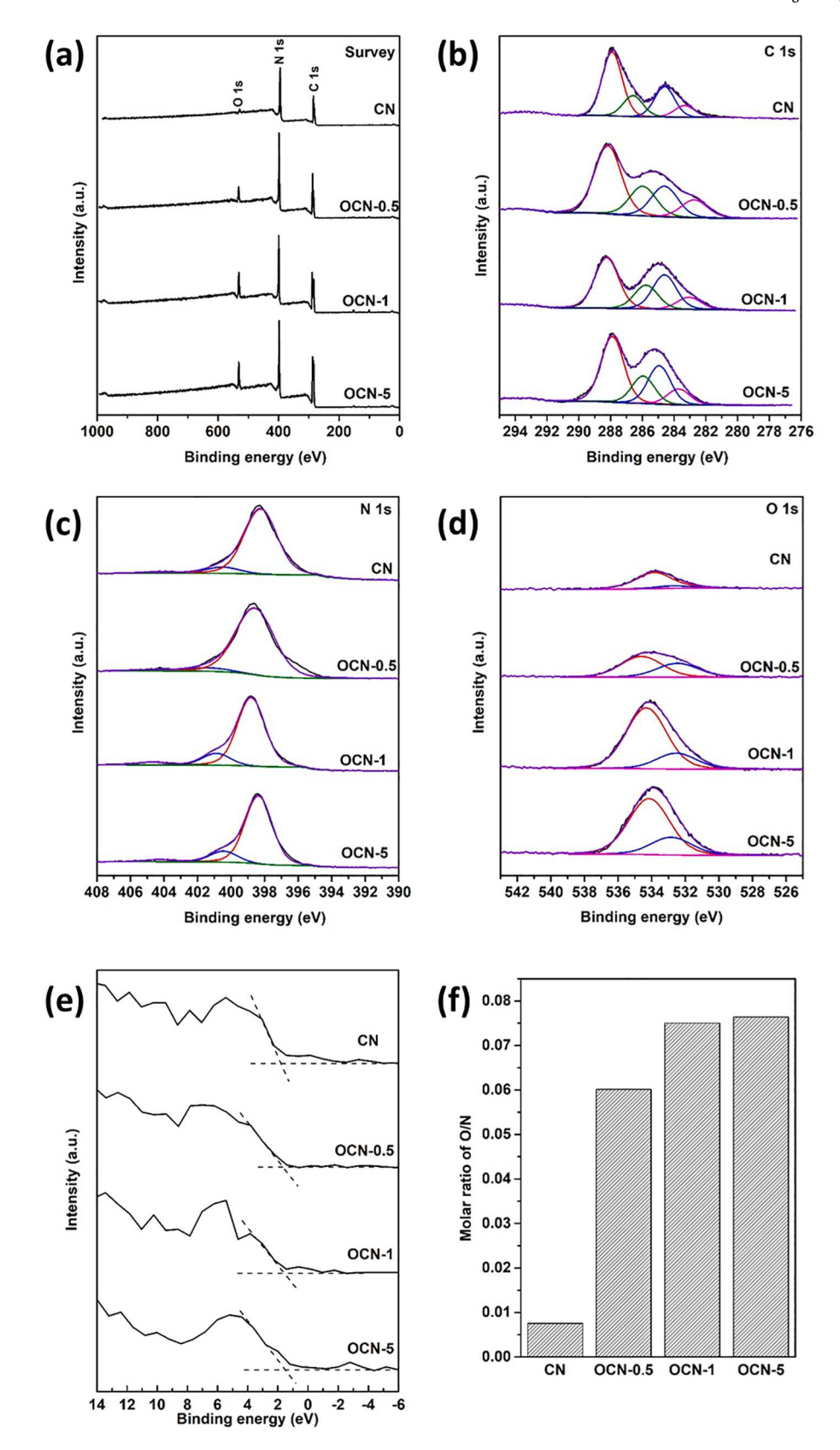


Fig. 4. XPS spectra of CN, OCN-0.5, OCN-1, and OCN-5: (a) survey spectra, (b) C 1 s, (c) N 1 s, (d) O 1 s, (e) valence band energy region, and (f) molar ratio of O/N.

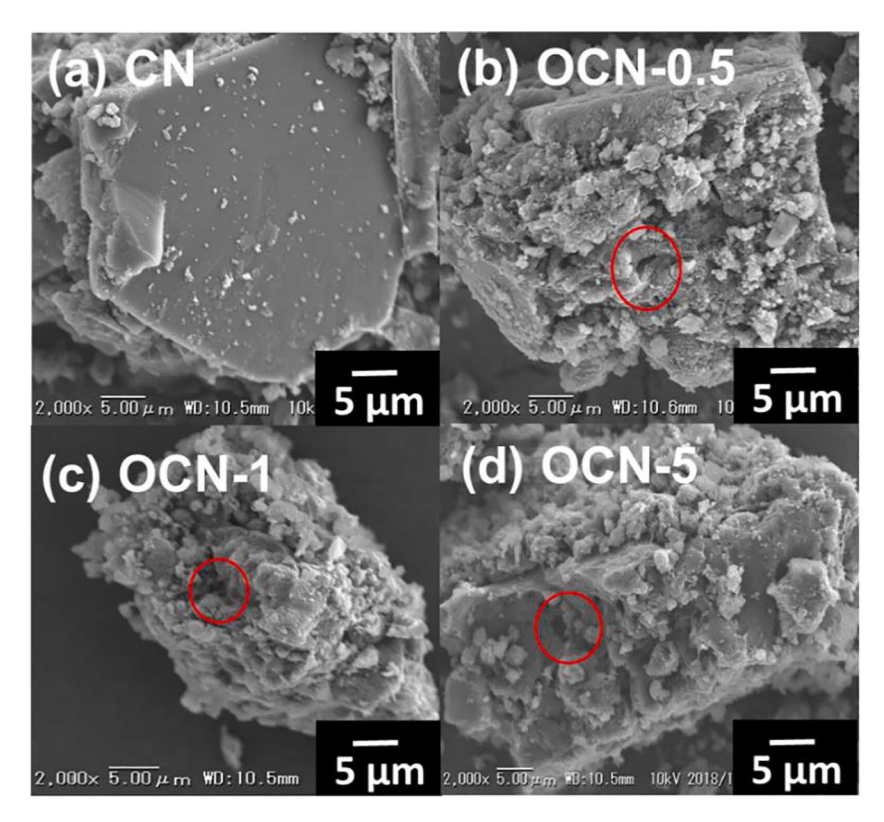


Fig. 5. SEM images of (a) CN, (b) OCN-0.5, (c) OCN-1, and (d) OCN-5.

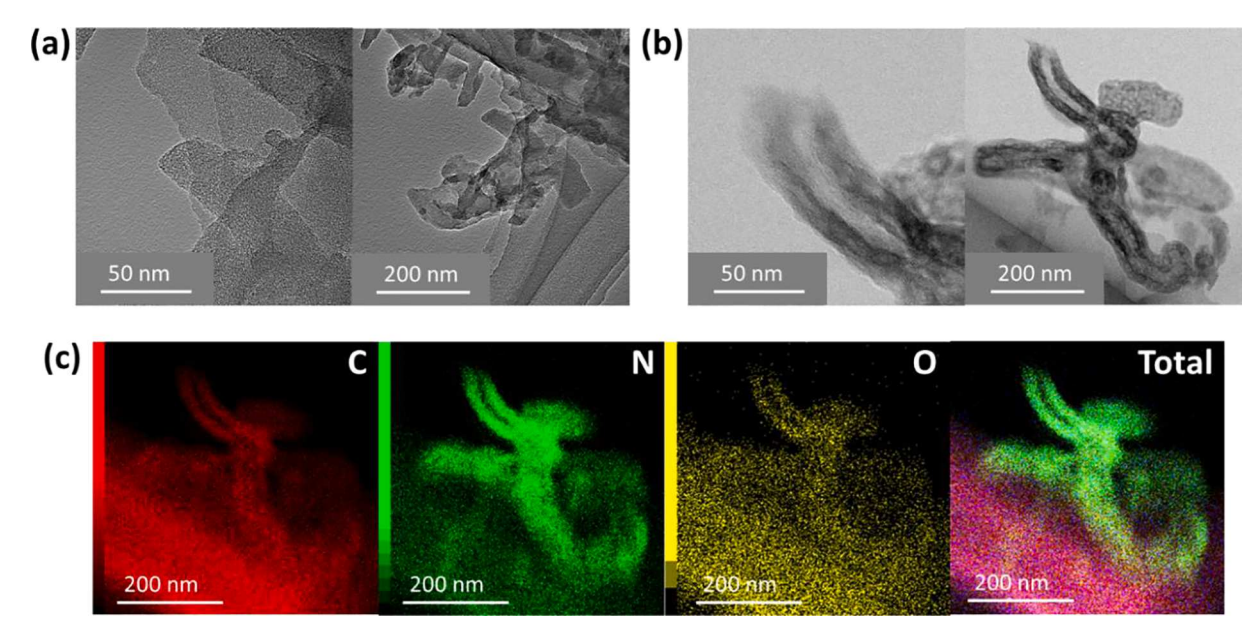


Fig. 6. TEM images of (a) pure CN, (b) OCN-1, and (c) TEM-EDX image of OCN-1.

# 3.7. ERDT results

To further confirm O doping in the  $C_3N_4$  structure, RDB-PAS—and the resulting ERDT pattern—was used as a fingerprint of  $C_3N_4$  [40,48]. In Fig. 7, the ERDT patterns of the samples exhibit a large accumulation of electrons near the conduction band bottom (CBB) at approximately 2.4–3.0 eV, suggesting that excited electrons can be trapped in the electron trap states close to the CBB. Compared to the CN sample, OCN-0.5 and OCN-1 exhibit high electron accumulation at approximately 2.4 eV, as the O doping in  $C_3N_4$  can generate an electron trap level below the

CBB. The presence of a new electronic level at approximately 2.4 eV caused by the extra electrons generated by the substitution of O into N sites in  $C_3N_4$  has previously been reported [40,49]. This extra electron trap level is less distinct in OCN-5 due to its high light absorption at 625 nm which affects the detection of electron accumulation through RDB-PAS. These results are well supported by the XPS and TEM results, confirming the successful introduction of O into the  $C_3N_4$ .

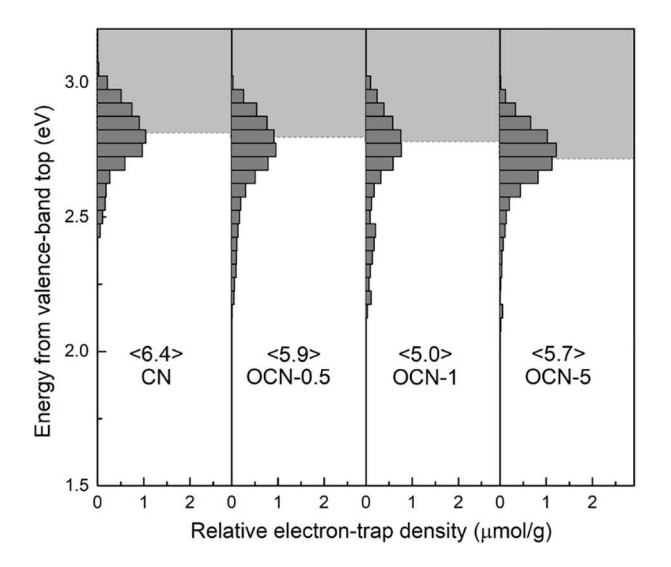


Fig. 7. Representative ERDT/ CBB patterns of the CN and OCN samples including relative total electron trap density in brackets.

# 3.8. DFT calculations

The band structure and PDOS of the CN and OCN samples were calculated to elucidate the electronic properties of O-doped C<sub>3</sub>N<sub>4</sub>. Fig. 8a shows the simulated, pristine monolayer of CN with a predicted  $E_g$  of 2.78 eV, which is close to the experimental UV-DRS values (Fig. 2b). Compared with pure CN, the OCN sample exhibits n-type doping with the formation of a new electron trapping level near the CB edge, as shown in Fig. 8b. Since an O atom has one more valence electron than a N atom, the substitution of O at N sites generates extra electrons. Further, a new fermi level is formed between the valence band top (VBT) and CBB due to the O atoms, as described in previous reports [40,49]. These gap states result in a reduced band gap of 2.4 eV for OCN. The predicted decrease in  $E_g$  corroborates the DRS experimental results. The presence of a new electronic level near the CBB in the DOS of OCN may explain the appearance of the electron trap state that was observed in the ERDT measurements (Fig. 7). Thus, the band structure and PDOS results obtained from DFT calculations provide further validation of the DRS and ERDT results and help to elucidate the critical impact of O doping on the optical and electronic properties of C<sub>3</sub>N<sub>4</sub>.

## 3.9. Photocatalytic performance for CIP degradation

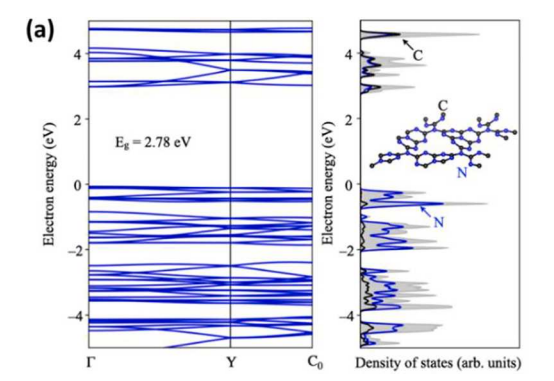
The photocatalytic performance of the CN and OCN samples were examined towards CIP degradation as shown in Fig. 9a. CIP adsorption of approximately 10% is observed on the surface of the CN and OCN

samples 30 min before light irradiation. The adsorption kinetic of CIP over OCN-1 was examined, as shown in Fig. S3. Adsorption-desorption equilibrium was achieved after 2 min, indicating that leaving the samples in the dark for 30 min was enough to achieve adsorption—desorption equilibrium. After a reaction time of 20 min, the degradation efficiency (C/C<sub>0</sub>) of CIP over CN, OCN-0.5, OCN-1, and OCN-5 was 0.38, 0.18, 0.06 and 0.23, respectively, corresponding to degradation activity of 62%, 82%, 95% and 77%. The O-doped samples showed significantly higher photocatalytic degradation of CIP, with OCN-1 exhibiting the best photocatalytic performance.

The improved photocatalytic efficiency of the OCN samples is caused by the prolonged life of the photogenerated charges carriers. In addition, the kinetics of the photocatalytic CIP decomposition were analyzed using a pseudo-first-order kinetic model:

$$-\ln(C/C_0) = kt, (2)$$

where  $C_0$ , t, C, and k are the original CIP concentration, reaction time (min), final CIP concentration at time t, and rate constant (min<sup>-1</sup>), respectively. The results were fitted by a linear plot of  $-\ln(C/C_0)$  against t, as shown in Fig. 9b. The photocatalytic degradation of CIP adheres to the pseudo-first-order kinetics reaction principle with correlation coefficients (R<sup>2</sup>) >0.93. The reaction rate constants of CN, OCN-0.5, OCN-1, and OCN-5 were 0.043, 0.073, 0.122, and 0.065 min<sup>-1</sup>, respectively. The highest rate constant was achieved by OCN-1, which is approximately three times higher than CN. These results confirm that OCN-1 has an optimal O concentration, leading to improved degradation of CIP. However, the photocatalytic activity toward the degradation of CIP decreased in OCN-5, which has the highest O content in the structure, indicating that large amounts of O result in excess defects in the C<sub>3</sub>N<sub>4</sub> structure, leading to poor performance in separating electron-hole pairs. Therefore, the results prove that the modification of C<sub>3</sub>N<sub>4</sub> with an appropriate number of O atoms can significantly enhance the photocatalytic degradation of CIP. Furthermore, the improvement in the degradation performance and reaction rate constant of CIP for the OCN samples suggest that O atoms in the C<sub>3</sub>N<sub>4</sub> structure could prevent electron-hole recombination, promote electron transport, and enhance light absorption. Moreover, the effect of the pH of the solution was investigated using OCN-1, as shown in Fig. 9e. From previous reports, C<sub>3</sub>N<sub>4</sub> has a pHzpc of 5.04 [50], while CIP has four pKa values at 3.01, 6.14, 8.70 and 10.58 (Fig. S4) [51]. At a pH of three, low photocatalytic CIP degradation efficiency was observed because of the repulsion between the positive charge of CIP and the positive surface charge of OCN-1. The photocatalytic activity improved as the pH increased to six and eight because the surface charge of OCN-1 became negative, resulting in excellent interactions with the positive CIP molecules. However, the degradation performance dropped at a pH of ten because the CIP molecule had less positive and negative sites which caused charge repulsion with the negative surface of OCN-1.



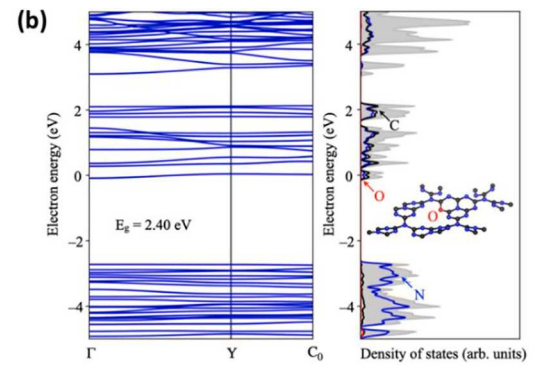
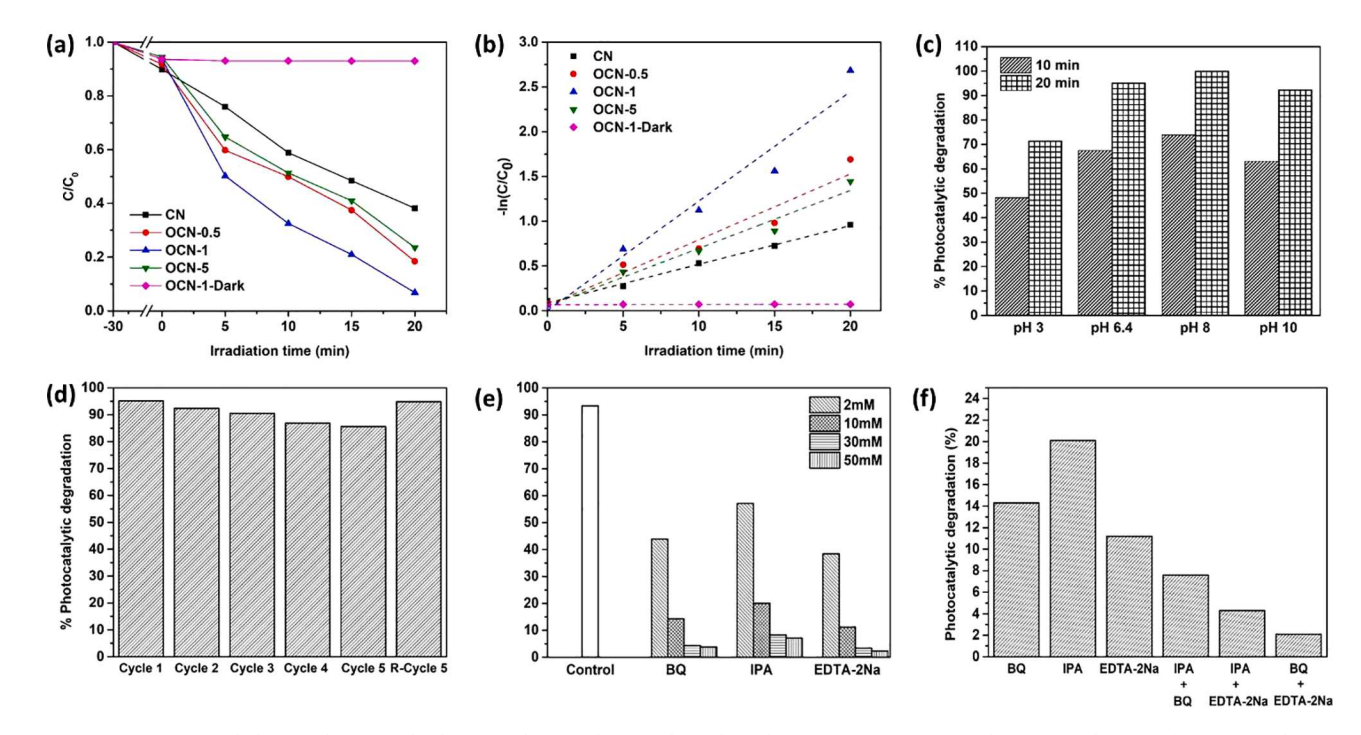


Fig. 8. Band structures and PDOS of (a) CN and (b) OCN. Electron energy is referenced to the Fermi level. Substitution of O in the  $C_3N_4$  structure causes n-type doping with a Fermi level close to the CB. The HSE06 calculations predict band gaps of 2.78 and 2.4 eV for the pristine and O-doped  $C_3N_4$ , respectively.



**Fig. 9.** (a) Time course and (b) pseudo-first-order kinetics plots of photocatalytic degradation of CIP over CN and OCN samples, (c) effect of initial pH on the photocatalytic degradation of CIP over OCN-1 (dosage = 1 g/L, CIP = 10 mg/L), (d) Photocatalytic degradation of CIP through five cycles, (e) degradation efficiency of CIP over OCN-1 for 20 min with various radical scavengers and (f) degradation efficiency of CIP over OCN-1 for 20 min with single and binary radical scavengers.

The reusability of OCN-1 was examined under the same conditions as CIP degradation. The spent catalyst was directly used during the next cycle without any treatment. Fig. 9d displays the CIP degradation over OCN-1 across five cycles. The photocatalytic activity is maintained at over 85% across all cycles, suggesting the stability of OCN-1 for the degradation of CIP. The decrease in photocatalytic CIP degradation may have been caused by a loss of catalyst during each cycle and the adsorption of organic byproducts on the surface of the OCN-1. Therefore, after the 5th cycle, the catalyst was regenerated by re-calcination at 400 °C for 30 min under ambient conditions to remove some of the organic byproduct. The photocatalytic performance of spent OCN-1 improved after regeneration and the efficiency was comparable to fresh OCN-1, indicating that heat treatment after CIP degradation can improve the reusability of OCN-1.

The stability of the photocatalyst was investigated by collecting XRD patterns of spent OCN-1 after first cycle of photocatalytic CIP decomposition, as shown in Fig. S5. The spent OCN-1 exhibits an XRD pattern similar to that of fresh OCN-1, containing two main diffraction peaks at

 $12.9^{\circ}$  and  $27.6^{\circ}$ , corresponding to the  $(1\,00)$  and  $(0\,0\,2)$  planes of  $C_3N_4$ , respectively; this indicates the high stability of  $C_3N_4$  after CIP degradation. Therefore, OCN-1 can be applied to the organic remediation of contaminated wastewater. Table 1 shows a comparison of  $C_3N_4$  photocatalysts obtained in the current and previous studies. In the present study, OCN-1 exhibits the highest photocatalytic performance toward CIP degradation, with a relatively short reaction time. Comparatively, OCN-1 exhibited excellent photocatalytic decomposition of CIP of approximately 95% within 20 min. Some previous works achieve higher degradation toward CIP (over 97%); however, the reaction times are significantly longer, making OCN-1 more useful for practical wastewater management.

# 3.10. Verification of active species and charge separation

To confirm the role of the active species generated during photocatalytic CIP degradation over OCN-1, radical scavenger experiments were performed. In previous reports, IPA, BQ, and EDTA-2Na were used

Table 1
Comparison of the degradation efficiency over different C<sub>2</sub>N<sub>4</sub> photocatalysts.

Entry	Photocatalysts	Photocatalytic test conditions	Irradiation time (min)	Degradation (%)	k (min <sup>-1</sup> )	Ref.
1	$\text{g-C}_3\text{N}_4/\text{RGO/WO}_3$	Catalyst loading = 0.2 g/L CIP concentration = 20 ppm Light source = 500 W high-pressure xenon short arc lamp	180	85	-	[52]
2	sepiolite/g- $C_3N_4$ /Pd	Catalyst loading = 0.4 g/L CIP concentration = 10 ppm Light source = 500 W Xe lamp with a cutoff filter ( $\lambda > 380 \text{ nm}$ )	60	64	0.016	[48]
3	g-C <sub>3</sub> N <sub>4</sub> /TiO <sub>2</sub> (10%)	Catalyst loading = 0.4 g/L CIP concentration = 10 ppm Light source = 300 W Xe arc lamp equipped with an ultraviolet filter ( $\lambda > 400 \text{ nm}$ )	180	88.1	-	[53]
4	Kaolin-Supported g- C <sub>3</sub> N <sub>4</sub> /CeO <sub>2</sub>	Catalyst loading = 1 g/L CIP concentration = 20 ppm Light source = 500 W Xenon lamp with a UV-cutoff filter ( $\lambda > 420$ nm)	150	90	0.010	[54]
5	g-C <sub>3</sub> N <sub>4</sub> /Bi <sub>2</sub> WO <sub>6</sub>	Catalyst loading = 1 g L CIP concentration = 15 ppm Light source = 300 W Xenon lamp with a UV-cutoff filter ( $\lambda > 400$ nm)	120	97.8	-	[55]
6	$\text{g-C}_3\text{N}_4/\text{Ti}_3\text{C}_2$	Catalyst loading = 1 g/L CIP concentration = 20 ppm Light source = 300 W Xenon lamp with a UV-cutoff filter ( $\lambda > 400$ nm)	150	100	0.035	[56]
7	OCN-1	Catalyst loading = 1 g/L CIP concentration = 10 ppm Light source = 500 W Xe lamp with a UV-cutoff filter ( $\lambda > 380$ nm)	20	95	0.122	Present work

as the hydroxyl radical, superoxide radical, and hole scavengers, respectively [11,18,57]. Generally, each radical scavenger can quickly react with and remove the target active radical, resulting in a decrease in the degradation activity. Thus, the decreasing of photocatalytic activity in the presence of radical scavengers can confirm the role of each target radical. As shown in Fig. 9e, the photocatalytic activity of CIP decreases when EDTA-2Na, BQ and IPA were added in to the reaction. In addition, when the concentration of scavenger reagent increase, the degradation efficiency decrease because the important active radicals in the reaction was quenching from the reaction solution. These results suggest the  ${}^{\bullet}O_2^-$ , OH and h+ play important role for the CIP degradation. Moreover, mixing of two type of scavengers such as IPA with BQ, IPA with EDTA-2Na and EDTA-2Na with BQ, were studied compare with single scavenger system to emphasize role of  $\bullet O_2^-$ ,  $\bullet OH$  and  $h^+$ . In Fig. 9f, the mixing of IPA with BQ show lower photocatalytic CIP degradation performance than IPA and BQ alone, while the lower CIP degradation can be observed in the case of mixing between IPA with EDTA-2Na compare with the single IPA and EDTA-2Na. The lowest photocatalytic activity was obtained when the mixing of BQ and EDTA-2Na was used. The different between single and binary system of scavengers emphasize the role of BQ and EDTA-2Na as  $\bullet O_2^-$  and  $h^+$  scavengers. From these results,  $\bullet O_2^-$ ,  $\bullet OH$  and  $h^+$  are jointly participated in the CIP degradation.

To investigate the recombination and transfer of electron-hole pairs, PL spectroscopy, photocurrent spectroscopy, and electrochemical impedance spectroscopy (EIS) were carried out. Fig. 10a shows the PL emission spectra of the CN and OCN samples, with peak emission occurring at approximately 450 nm under a light excitation of 370 nm. Compared with the CN sample, the PL intensity of all OCN samples significantly decreased, with the lowest PL intensity obtained from OCN-1. This suggests that O doping can reduce the recombination rate by generating a new electron trapping state, as confirmed by the ERDT results, resulting in improved photocatalytic activity. However, the high O content of OCN-5 increased the PL intensity, suggesting that an excess of new electron trap levels has adverse effects on electron-hole recombination centers [58,59], thereby reducing the electron-hole pair separation efficiency and photocatalytic activity.

The excellent charge separation of OCN-1 is further confirmed by the transient photocurrent response shown in Fig. 10b. OCN-1 clearly exhibits the highest photocurrent density, indicating that this sample has optimal O content and can achieve a high charge separation. The separation and transfer of electron-hole pairs were determined using EIS measurement. A smaller arc radius in the EIS Nyquist diagram implies faster transfer of the electrons. From Fig. 10c, the size of the arc radius follows the order: CN > OCN-5 > OCN-0.5 > OCN-1. The high charge separation and transfer of the OCN samples may be caused by the formation of a defect state caused by the replacement of a N atom with an O atom; this defect can trap photogenerated electrons, enhancing the transportation and separation of photogenerated charge carriers [49]. Thus, the O-doped hollow porous  $C_3N_4$  had improved charge recombination and transfer, resulting in the enhanced photocatalytic efficiency

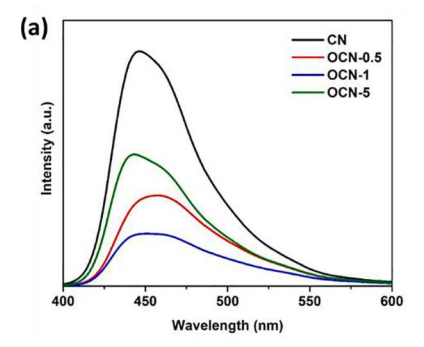
of CIP degradation.

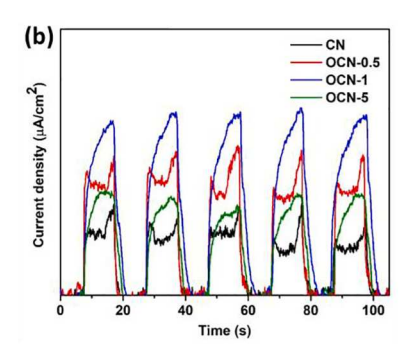
# 3.11. Possible photocatalytic degradation pathway of CIP

The suggested photocatalytic degradation pathway of CIP is proposed based on relevant literature and the detection of the intermediate products by liquid chromatography-mass spectrometry (LC-MS) analysis during the photocatalytic reaction of OCN-1 (Fig. S2). Scheme 1 shows the suggested photocatalytic decomposition pathway of CIP over OCN-1, with four major transformation pathways. Pathway 1 starts from the destruction of the piperazine ring, followed by the elimination of CO groups, decarboxylation, and decarbonylation. From the LC-MS results, intermediate products at m/z 245 (F1) and m/z 219 (F2) are detected, confirming the complete distortion of the piperazinyl substituent of CIP during this process. The second CIP degradation route starts with the removal of the fluorine ion, followed by the decomposition of the piperazine ring. The molecular ions m/z 205 (F3), m/z 231 (F4), m/z 217 (F5), m/z 201 (F6), m/z 302 (F7), and m/z 256 (F8) are observed, which are the products of defluorination, removal of the piperazine ring, and loss of the NH and COO groups [60-62]. The third degradation route begins with the breaking down of the aromatic ring of the CIP molecule, following by defluorination and hydroxylation, confirmed by the detection of small molecules with m/z 188 (F9) and m/z 104 (F10) [63]. Moreover, the detection of small molecules with m/z 112 (F11) and m/z118 (F12) suggests the hydrolysis and hydroxylation of the CIP molecule, which is proposed in the fourth degradation route [63]. In addition, from the LC-MS spectrum in Fig. S2, the main peaks are assigned to the small molecules F11 and F12, which have no toxic or antibacterial components (such as fluorine, quinolone and piperazine rings) in their structure [64], suggesting that the degradation of CIP over OCN-1 not only degrades the CIP molecule, but also decreases the toxicity of the final products. Therefore, the presence of the intermediate products confirms the degradation of CIP through photocatalytic treatment. Moreover, the number of fluoride ions in the final solution after photocatalytic CIP degradation over OCN-1 for 20 min was investigated, as shown in Fig. S6. After photocatalysis, the solution contained 0.24 ppm of fluoride ions, which is lower than the recommended level for drinking water from the Environmental Protection Agency (EPA; less than 1 ppm) [65]. These results confirm the defluorination of CIP and suggest that the degraded solution may have lower toxicity than the fresh CIP solution.

# 3.12. Bio-toxicity of degraded CIP solution

The bio-toxicity of the degraded CIP solution was evaluated by observation of the growth of *E. coli* in degraded CIP solution compared with untreated CIP solution and water. Fig. 11 shows the MC-media pad with water and *E. coli* before incubation (Fig. 11a) and the growth of the *E. coli* after incubation in different solutions: water (control; Fig. 11b), CIP solution (Fig. 11c) and CIP solution degraded over OCN-1 for 20 min





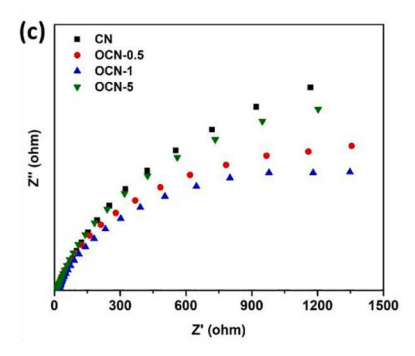
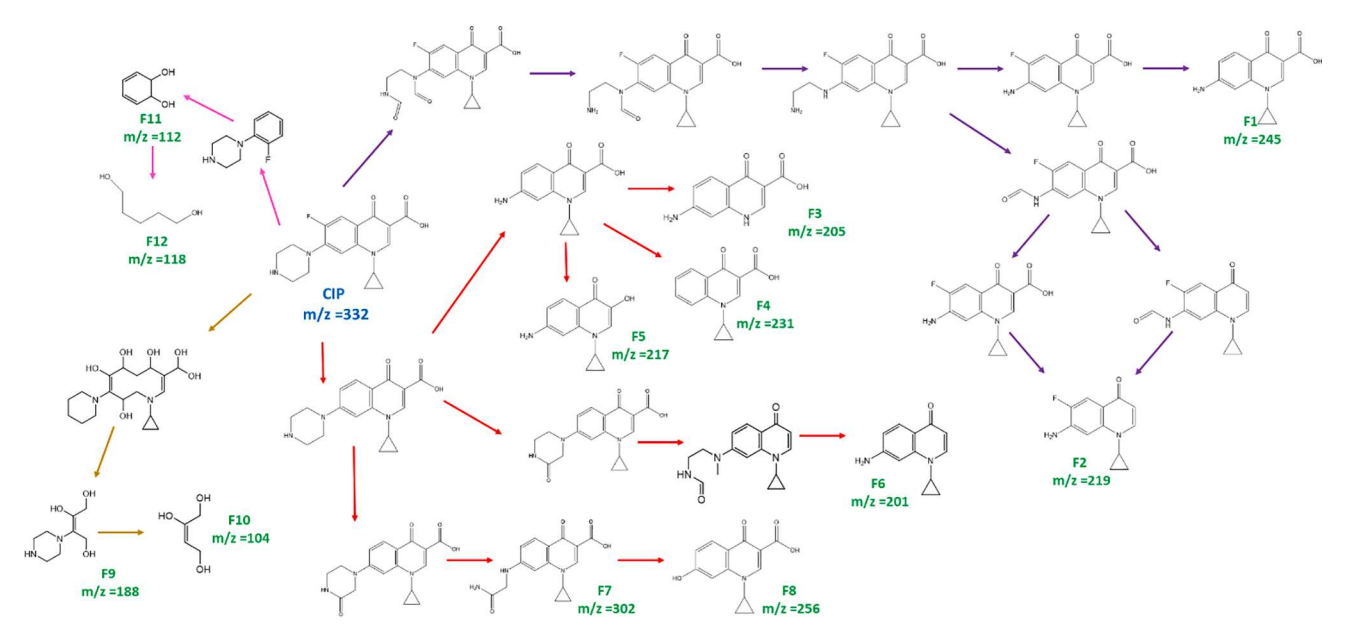


Fig. 10. (a) PL spectra, (b) photocurrent response, and (c) EIS spectra of pure CN, OCN-0.5, OCN-1, and OCN-5.



Scheme 1. Photocatalytic degradation pathways of CIP over OCN-1. Obtained using LC-MS.

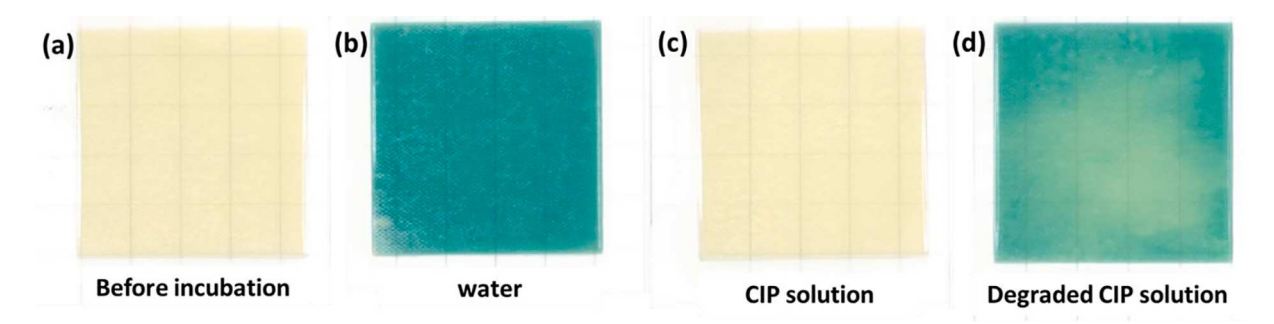
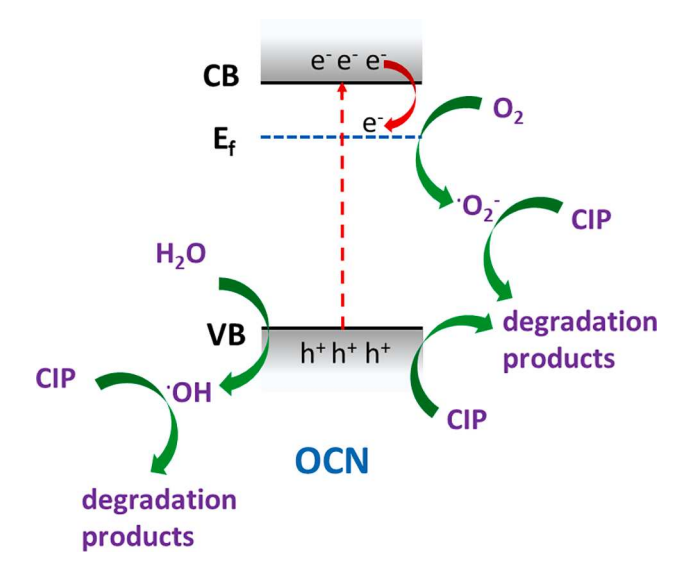


Fig. 11. Growth of E. coli on an MC-media pad with (a) water before incubation, and (b) water, (c) CIP solution, and (d) degraded CIP solution after incubation.

(Fig. 11d). The appearance of blue indicates the growth and survival of E.coli. It can be seen that the control MC-media pad is blue after incubation, suggesting that the pad is suitable for the growth of E. coli. Interestingly, no blue areas can be seen in the presence of the CIP solution because CIP is a drug which can inhibit the growth of E. coli. However, an E. coli colony was observed around the rim of the MCmedia pad of the degraded CIP solution, indicating a significant decrease in the harmfulness of the solution after photocatalysis. From a previous report, the fluorine, quinolone and piperazine ring of CIP molecules are essential to its antibacterial properties [64]. Thus, the defluorination and degradation of the CIP molecules over OCN-1 could decrease the toxicity of CIP in wastewater. Furthermore, the TOC of the CIP solution degraded over OCN-1 was also examined. In Fig. S7, the TOC removal efficiency was approximately 4.5% after adsorption in dark conditions and 60.7% after photocatalytic treatment, indicating that the photocatalysis of CIP not only degrades, but also mineralizes the CIP molecules, resulting in a decreased C content in the final solution.

## 3.13. Photocatalytic mechanism

A possible photocatalytic CIP degradation route by OCN-1 was proposed, as shown in Scheme 2. OCN-1 has an  $E_g$  of approximately 2.77 eV. From the XPS results, the VB and CB of OCN-1 are 1.62 and - 1.15 eV, respectively. The ERDT results and DFT calculation suggest the formation of a new electronic state near the CBB. Thus, under light irradiation, an electron is generated and transferred to the CB, while simultaneously producing a photogenerated  $h^+$  in the VB. The electron from the CB can



Scheme 2. Photocatalytic degradation mechanism of CIP using OCN.

migrate to a new electron trap state created by the O atoms to reduce the electron-hole recombination. The electron in this state can react with the dissolved  $O_2$  in the  $H_2O$  to produce  ${}^\bullet O_2^-$  as it is more negative than the reduction potential of the production of  $O_2$  (-0.046 eV) against a

normal hydrogen electrode. Meanwhile, some of the  ${}^{\bullet}O_2^-$  reacts with  $H^+$  and  $e^-$  to generate  ${}^{\bullet}OH$ , which could be produced by the decomposition of  $H_2O$  by reacting with  $h^+$  in the VB. Moreover,  $h^+$  in the VB can directly oxidize the CIP molecules. Thus, these active species contribute to CIP decomposition. Therefore, the degradation pathways of CIP over the OCN sample could be described the following reactions.

$$OCN + h\nu \rightarrow OCN (h_{VB}^{+} + e_{CB}^{-})$$
(3)

$$OCN (e_{CB}^{-}) + O_2 \rightarrow {}^{\bullet}O_2^{-}$$
(4)

$${}^{\bullet}\text{O}_{2}^{-} + \text{H}^{+} \rightarrow {}^{\bullet}\text{OOH}$$
 (5)

$$^{\bullet}OOH + H^{+} + e^{-} \rightarrow H_{2}O_{2}$$
 (6)

$$H_2O_2 + e^- \rightarrow {}^{\bullet}OH + OH^- \tag{7}$$

$$H_2O + CN (h^+)^- \to {}^{\bullet}OH + H^+$$
 (8)

$$^{\bullet}$$
OH + CIP  $\rightarrow$  degraded products (9)

$$^{\bullet}\text{O}_2^- + \text{CIP} \rightarrow \text{degraded products}$$
 (10)

$$CN(h^+) + CIP \rightarrow degraded products$$
 (11)

#### 4. Conclusions

OCN was successfully synthesized by the polycondensation of melamine with polyoxyethylene stearyl ether as the template and coprecursor. The utilization of an O-containing template not only changed the morphology of C<sub>3</sub>N<sub>4</sub> from a smooth sheet to a hollow porous structure, but also improved its optical properties, such as narrowing  $E_g$  and enhancing the visible light absorption by generating a new electron trap state. Furthermore, the presence of O atoms in the C<sub>3</sub>N<sub>4</sub> structure encouraged the transfer and separation of charge carriers, resulting in the generation of more active radicals, thereby enhancing photocatalytic CIP decomposition. The highest activity toward CIP degradation (approximately 95% within 20 min) was achieved over OCN-1, which was found to be the optimal sample. The highly improved activity of OCN was ascribed to its high SSA, low recombination, and high charge transfer. Thus, this work may provide new insights into the production of heteroatom-doped hollow porous C<sub>3</sub>N<sub>4</sub> with high photocatalytic activity through single-step synthesis.

# CRediT authorship contribution statement

Chitiphon Chuaicham: Conceptualization, Investigation, Formal analysis, Writing - original draft, Writing - review & editing. Karthikeyan Sekar: Formal analysis. Yihuang Xiong: Software, Formal analysis. Vellaichamy Balakumar: Formal analysis. Yanisa Mittraphab: Formal analysis. Kuniyoshi Shimizu: Investigation. Bunsho Ohtani: Investigation. Ismaila Dabo: Investigation. Keiko Sasaki: Conceptualization, Funding acquisition, Investigation, Project administration, Supervision, Validation, Visualization, Writing - review & editing.

# **Declaration of Competing Interest**

The authors declare that they have no known competing financial interests or personal relationships that could have appeared to influence the work reported in this paper.

# Acknowledgements

The authors would like to thank the Nanotech Center, Kyushu University for the XPS measurements; HVEM Center, Kyushu University for the TEM-EDX; and Penn State Institute of Computational and Data

Sciences for providing the high-performance computing resources for the computational work. The authors thank Dr. Wang Dongmei for helping during the LC-MS analysis.

# Funding

The work was supported by the Japan Society for the Promotion of Science (JSPS) KAKENHI (A) [No. JP19F19393]; Cooperative Research Programs at Hokkaido University Institute for Catalysis [Nos. 18A1001, 19B1002, 20A1001 and 21A1001]; and Kyushu University (Progress 100) to KS; and the National Science Foundation (NSF) [grant No. DMREF-1729338] to ID. This work was supported by nanotech platform with the proposal No. S-20-KU-0001. The funding source(s) was (were) not involved in the study design; in the collection, analysis, and interpretation of data; in the writing of the report; and in the decision to submit the article for publication.

#### Appendix A. Supplementary data

Supplementary data to this article can be found online at https://doi.org/10.1016/j.cej.2021.130502.

#### References

- X. Yang, D. Wang, Photocatalysis: From fundamental principles to materials and applications, ACS Applied Energy Materials 1 (12) (2018) 6657–6693, https://doi. org/10.1021/acsaem.8b01345.
- [2] S. Karthikeyan, C. Chuaicham, R.R. Pawar, K. Sasaki, W. Li, A.F. Lee, K. Wilson, Template free mild hydrothermal synthesis of core-shell Cu2O(Cu)@CuO visible light photocatalysts for N-acetyl-para-aminophenol degradation, J. Mater. Chem. A 7 (36) (2019) 20767–20777, https://doi.org/10.1039/c9ta07009e.
- [3] K. Sekar, C. Chuaicham, U. Balijapalli, W. Li, K. Wilson, A.F. Lee, K. Sasaki, Surfactant- and template-free hydrothermal assembly of Cu2O visible light photocatalysts for trimethoprim degradation, Appl. Catal. B 284 (2021), 119741.
- [4] K. Sekar, C. Chuaicham, B. Vellaichamy, W. Li, W. Zhuang, X. Lu, B. Ohtani, K. Sasaki, Cubic Cu2O nanoparticles decorated on TiO2 nanofiber heterostructure as an excellent synergistic photocatalyst for H2 production and sulfamethoxazole degradation, Appl. Catal. B 294 (2021), 120221.
- [5] H. Huang, J. Zhang, L. Jiang, Z. Zang, Preparation of cubic Cu2O nanoparticles wrapped by reduced graphene oxide for the efficient removal of rhodamine B, J. Alloy. Compd. 718 (2017) 112–115.
- [6] Y. Ye, Z. Zang, T. Zhou, F. Dong, S. Lu, X. Tang, W. Wei, Y. Zhang, Theoretical and experimental investigation of highly photocatalytic performance of CuInZnS nanoporous structure for removing the NO gas, J. Catal. 357 (2018) 100–107.
- [7] M.Q. Wen, T. Xiong, Z.G. Zang, W. Wei, X.S. Tang, F. Dong, Synthesis of MoS2/g-C3N4 nanocomposites with enhanced visible-light photocatalytic activity for the removal of nitric oxide (NO), Opt. Express 24 (10) (2016) 10205–10212, https:// doi.org/10.1364/OE.24.010205.
- [8] X. Wang, S. Blechert, M. Antonietti, Polymeric Graphitic Carbon Nitride for Heterogeneous Photocatalysis, ACS Catal. 2 (8) (2012) 1596–1606, https://doi. org/10.1021/cs300240y
- [9] B. Vellaichamy, P. Periakaruppan, Synergistic combination of a novel metal-free mesoporous band-gap-modified carbon nitride grafted polyaniline nanocomposite for decontamination of refractory pollutant, Ind. Eng. Chem. Res. 57 (19) (2018) 6684–6695, https://doi.org/10.1021/acs.iecr.8b0109810.1021/acs.iecr.8b01098.
- [10] C. Jin, M. Wang, Z. Li, J. Kang, Y. Zhao, J. Han, Z. Wu, Two dimensional Co3O4/g-C3N4 Z-scheme heterojunction: Mechanism insight into enhanced peroxymonosulfate-mediated visible light photocatalytic performance, Chem. Eng. J. 398 (2020), 125569.
- [11] M. Dou, J. Wang, B. Gao, C. Xu, F. Yang, Photocatalytic difference of amoxicillin and cefotaxime under visible light by mesoporous g-C3N4: Mechanism, degradation pathway and DFT calculation, Chem. Eng. J. 383 (2020), 123134.
- [12] Q. Tang, Z. Sun, S. Deng, H. Wang, Z. Wu, Decorating g-C3N4 with alkalinized Ti3C2 MXene for promoted photocatalytic CO2 reduction performance, J. Colloid Interface Sci. 564 (2020) 406–417.
- [13] Y.-C. Chu, T.-J. Lin, Y.-R. Lin, W.-L. Chiu, B.-S. Nguyen, C. Hu, Influence of P, S, O-Doping on g-C3N4 for hydrogel formation and photocatalysis: An experimental and theoretical study, Carbon 169 (2020) 338–348.
- [14] S. Cao, Q. Huang, B. Zhu, J. Yu, Trace-level phosphorus and sodium co-doping of g-C3N4 for enhanced photocatalytic H2 production, J. Power Sources 351 (2017) 151–159.
- [15] F. Nekouei, S. Nekouei, M. Pouzesh, Y. Liu, Porous-CdS/Cu2O/graphitic-C3N4 dual p-n junctions as highly efficient photo/catalysts for degrading ciprofloxacin and generating hydrogen using solar energy, Chem. Eng. J. 385 (2020), 123710.
- [16] B. Ou, J. Wang, Y. Wu, S. Zhao, Z. Wang, Efficient removal of Cr (VI) by magnetic and recyclable calcined CoFe-LDH/g-C3N4 via the synergy of adsorption and photocatalysis under visible light, Chem. Eng. J. 380 (2020), 122600.

- [17] Z. Shi, Y. Zhang, X. Shen, G. Duoerkun, B. Zhu, L. Zhang, M. Li, Z. Chen, Fabrication of g-G3N4/BiOBr heterojunctions on carbon fibers as weaveable photocatalyst for degrading tetracycline hydrochloride under visible light, Chem. Eng. J. 386 (2020), 124010.
- [18] G. Zhao, J. Ding, F. Zhou, X. Chen, L. Wei, Q. Gao, K. Wang, Q. Zhao, Construction of a visible-light-driven magnetic dual Z-scheme BiVO4/g-C3N4/NiFe2O4 photocatalyst for effective removal of ofloxacin: Mechanisms and degradation pathway, Chem. Eng. J. 405 (2021), 126704.
- [19] Q. Liu, J. Shen, X. Yu, X. Yang, W. Liu, J. Yang, H. Tang, H. Xu, H. Li, Y. Li, J. Xu, Unveiling the origin of boosted photocatalytic hydrogen evolution in simultaneously (S, P, O)-Codoped and exfoliated ultrathin g-C3N4 nanosheets, Appl. Catal. B 248 (2019) 84–94.
- [20] Y. Chen, F. Su, H. Xie, R. Wang, C. Ding, J. Huang, Y. Xu, L. Ye, One-step construction of S-scheme heterojunctions of N-doped MoS2 and S-doped g-C3N4 for enhanced photocatalytic hydrogen evolution, Chem. Eng. J. 404 (2021), 126498
- [21] S. Patnaik, D.P. Sahoo, K. Parida, Recent advances in anion doped g-C3N4 photocatalysts: A review, Carbon 172 (2021) 682–711.
- [22] S. Wang, Y. Liu, J. Wang, Iron and sulfur co-doped graphite carbon nitride (FeOy/S-g-C3N4) for activating peroxymonosulfate to enhance sulfamethoxazole degradation, Chem. Eng. J. 382 (2020), 122836.
- [23] W. Wang, Z. Zeng, G. Zeng, C. Zhang, R. Xiao, C. Zhou, W. Xiong, Y. Yang, L. Lei, Y. Liu, D. Huang, M. Cheng, Y. Yang, Y. Fu, H. Luo, Y. Zhou, Sulfur doped carbon quantum dots loaded hollow tubular g-C3N4 as novel photocatalyst for destruction of Escherichia coli and tetracycline degradation under visible light, Chem. Eng. J. 378 (2019), 122132.
- [24] G. Liu, Z. Zhang, M. Lv, H. Wang, D. Chen, Y. Feng, Photodegradation performance and transformation mechanisms of sulfamethoxazole by porous g-C3N4 modified with ammonia bicarbonate, Sep. Purif. Technol. 235 (2020), 116172.
- [25] F. Guo, M. Li, H. Ren, X. Huang, K. Shu, W. Shi, C. Lu, Facile bottom-up preparation of Cl-doped porous g-C3N4 nanosheets for enhanced photocatalytic degradation of tetracycline under visible light, Sep. Purif. Technol. 228 (2019), 115770.
- [26] J. Fu, B. Zhu, C. Jiang, B. Cheng, W. You, J. Yu, Hierarchical Porous O-Doped g-C3N4 with Enhanced Photocatalytic CO2 Reduction Activity, Small 13 (15) (2017) 1603938
- [27] F. Wei, Y. Liu, H. Zhao, X. Ren, J. Liu, T. Hasan, L. Chen, Y. Li, B.-L. Su, Oxygen self-doped g-G3N4 with tunable electronic band structure for unprecedentedly enhanced photocatalytic performance, Nanoscale 10 (9) (2018) 4515–4522, https://doi.org/10.1039/C7NR09660G.
- [28] Q. Liang, X. Liu, J. Wang, Y. Liu, Z. Liu, L. Tang, B. Shao, W. Zhang, S. Gong, M. Cheng, Q. He, C. Feng, In-situ self-assembly construction of hollow tubular g-C3N4 isotype heterojunction for enhanced visible-light photocatalysis: Experiments and theories, J. Hazard. Mater. 401 (2021), 123355.
- [29] D. Zheng, C. Pang, Y. Liu, X. Wang, Shell-engineering of hollow g-C3N4 nanospheres via copolymerization for photocatalytic hydrogen evolution, Chem. Commun. 51 (47) (2015) 9706–9709, https://doi.org/10.1039/C5CC03143E.
- [30] M. Liang, T. Borjigin, Y. Zhang, B. Liu, H. Liu, H. Guo, Controlled assemble of hollow heterostructured g-C3N4@CeO2 with rich oxygen vacancies for enhanced photocatalytic CO2 reduction, Appl. Catal. B 243 (2019) 566–575.
- [31] T. Xiao, Z. Tang, Y. Yang, L. Tang, Y. Zhou, Z. Zou, In situ construction of hierarchical WO3/g-C3N4 composite hollow microspheres as a Z-scheme photocatalyst for the degradation of antibiotics, Appl. Catal. B 220 (2018) 417–428
- [32] Y. Tang, X. Wang, J. Chen, X. Wang, D. Wang, Z. Mao, Templated transformation of g-C3N4 nanosheets into nitrogen-doped hollow carbon sphere with tunable nitrogen-doping properties for application in Li-ions batteries, Carbon 168 (2020)
- [33] R.J. White, K. Tauer, M. Antonietti, M.-M. Titirici, Functional Hollow Carbon Nanospheres by Latex Templating, J. Am. Chem. Soc. 132 (49) (2010) 17360–17363, https://doi.org/10.1021/ja107697s.
- [34] L. Shi, F. Wang, J. Sun, The preparation of spherical mesoporous g-C3N4 with highly improved photocatalytic performance for H2 production and rhodamine B degradation, Mater. Res. Bull. 113 (2019) 115–121.
- [35] J. Sun, J. Zhang, M. Zhang, M. Antonietti, X. Fu, X. Wang, Bioinspired hollow semiconductor nanospheres as photosynthetic nanoparticles, Nat. Commun. 3 (1) (2012) 1139, https://doi.org/10.1038/ncomms2152.
- [36] G. Kresse, J. Furthmuller, Efficient iterative schemes for ab initio total-energy calculations using a plane-wave basis set, Physical review, B, Condensed matter 54 (16) (1996) 11169–11186, https://doi.org/10.1103/physrevb.54.11169.
- [37] J.P. Perdew, K. Burke, M. Ernzerhof, Generalized Gradient Approximation Made Simple, Phys Rev Lett 77 (18) (1996) 3865–3868, https://doi.org/10.1103/ PhysRevLett 77 3865
- [38] S. Grimme, Semiempirical GGA-type density functional constructed with a long-range dispersion correction, J Comput Chem 27 (15) (2006) 1787–1799, https://doi.org/10.1002/jcc.20495.
- [39] H.J. Monkhorst, J.D. Pack, Special Points for Brillouin-Zone Integrations, Physical Review B 13(12) (1976) 5188-5192. https://doi.org/DOI 10.1103/ PhysRevB.13.5188.
- [40] C. Chuaicham, S. Karthikeyan, R.R. Pawar, Y. Xiong, I. Dabo, B. Ohtani, Y. Kim, J. T. Song, T. Ishihara, K. Sasaki, Energy-resolved distribution of electron traps for O/S-doped carbon nitrides by reversed double-beam photoacoustic spectroscopy and the photocatalytic reduction of Cr(vi), Chem Commun (Camb) 56 (26) (2020) 3793–3796, https://doi.org/10.1039/c9cc09988c.
- [41] Y. Hinuma, G. Pizzi, Y. Kumagai, F. Oba, I. Tanaka, Band structure diagram paths based on crystallography, Comput. Mater. Sci. 128 (2017) 140–184.

- [42] A.V. Krukau, O.A. Vydrov, A.F. Izmaylov, G.E. Scuseria, Influence of the exchange screening parameter on the performance of screened hybrid functionals, J. Chem. Phys. 125 (22) (2006) 224106, https://doi.org/10.1063/1.2404663.
- [43] C. Chuaicham, R. Pawar, K. Sasaki, Dye-sensitized Photocatalyst of Sepiolite for Organic Dye Degradation, Catalysts 9(3) (2019) 235. https://doi.org/Artn 23510.3390/Catal9030235.
- [44] C. Chuaicham, S. Karthikeyan, J.T. Song, T. Ishihara, B. Ohtani, K. Sasaki, Importance of ZnTiO3 Phase in ZnTi-mixed metal oxide photocatalysts derived from layered double hydroxide, ACS Appl Mater Interfaces 12 (8) (2020) 9169–9180, https://doi.org/10.1021/acsami.9b18785.
- [45] C. Chuaicham, Y. Xiong, K. Sekar, W. Chen, L. Zhang, B. Ohtani, I. Dabo, K. Sasaki, A promising Zn-Ti layered double hydroxide/Fe-bearing montmorillonite composite as an efficient photocatalyst for Cr(VI) reduction: Insight into the role of Fe impurity in montmorillonite, Appl. Surf. Sci. (2020), 148835.
- [46] E. Samuel, B. Joshi, H.S. Jo, Y.I. Kim, S. An, M.T. Swihart, J.M. Yun, K.H. Kim, S. S. Yoon, Carbon nanofibers decorated with FeOx nanoparticles as a flexible electrode material for symmetric supercapacitors, Chem. Eng. J. 328 (2017) 776–784
- [47] H. Liu, D. Chen, Z. Wang, H. Jing, R. Zhang, Microwave-assisted molten-salt rapid synthesis of isotype triazine-/heptazine based g-C3N4 heterojunctions with highly enhanced photocatalytic hydrogen evolution performance, Appl. Catal. B 203 (2017) 300–313.
- [48] C. Chuaicham, R.R. Pawar, S. Karthikeyan, B. Ohtani, K. Sasaki, Fabrication and characterization of ternary sepiolite/g-C3N4/Pd composites for improvement of photocatalytic degradation of ciprofloxacin under visible light irradiation, J. Colloid Interface Sci. 577 (2020) 397–405.
- [49] J. Li, B. Shen, Z. Hong, B. Lin, B. Gao, Y. Chen, A facile approach to synthesize novel oxygen-doped g-C3N4 with superior visible-light photoreactivity, Chem. Commun. 48 (98) (2012) 12017–12019, https://doi.org/10.1039/C2CC35862J.
- [50] S.A. Younis, A. Abd-Elaziz, A.I. Hashem, Utilization of a pyrrole derivative based antimicrobial functionality impregnated onto CaO/g-C3N4 for dyes adsorption, RSC Adv. 6 (92) (2016) 89367–89379, https://doi.org/10.1039/C6RA10143G.
- [51] X. Hu, X. Hu, Q. Peng, L. Zhou, X. Tan, L. Jiang, C. Tang, H. Wang, S. Liu, Y. Wang, Z. Ning, Mechanisms underlying the photocatalytic degradation pathway of ciprofloxacin with heterogeneous TiO2, Chem. Eng. J. 380 (2020), 122366.
- [52] N. Lu, P. Wang, Y. Su, H. Yu, N. Liu, X. Quan, Construction of Z-Scheme g-C3N4/ RGO/WO3 with in situ photoreduced graphene oxide as electron mediator for efficient photocatalytic degradation of ciprofloxacin, Chemosphere 215 (2019) 444, 453
- [53] Z. Yang, J. Yan, J. Lian, H. Xu, X. She, H. Li, g-C3N4/TiO2 Nanocomposites for Degradation of Ciprofloxacin under Visible Light Irradiation, ChemistrySelect 1 (18) (2016) 5679–5685.
- [54] Z. Huang, L. Li, Z. Li, H. Li, J. Wu, Synthesis of Novel Kaolin-Supported g-C(3)N (4)/CeO(2) Composites with Enhanced Photocatalytic Removal of Ciprofloxacin, Materials (Basel) 13 (17) (2020) 3811, https://doi.org/10.3390/ma13173811.
- [55] J. Mao, B. Hong, J. Wei, J. Xu, Y. Han, H. Jin, D. Jin, X. Peng, J. Li, Y. Yang, J. Gong, H. Ge, X. Wang, Enhanced ciprofloxacin photodegradation of visible-light-driven Z-Scheme g-C3N4/Bi2WO6 nanocomposites and interface effect, ChemistrySelect 4 (46) (2019) 13716–13723.
- [56] N. Liu, N. Lu, Y. Su, P. Wang, X. Quan, Fabrication of g-C3N4/Ti3C2 composite and its visible-light photocatalytic capability for ciprofloxacin degradation, Sep. Purif. Technol. 211 (2019) 782–789.
- [57] J.H. Shah, M. Fiaz, M. Athar, J. Ali, M. Rubab, R. Mehmood, S.U.U. Jamil, R. Djellabi, Facile synthesis of N/B-double-doped Mn2O3 and WO3 nanoparticles for dye degradation under visible light, Environ. Technol. 41 (18) (2020) 2372–2381, https://doi.org/10.1080/09593330.2019.1567604.
- [58] Y. Zhu, R. Zhu, G. Zhu, M. Wang, Y. Chen, J. Zhu, Y. Xi, H. He, Plasmonic Ag coated Zn/Ti-LDH with excellent photocatalytic activity, Appl. Surf. Sci. 433 (2018) 458–467.
- [59] T. Xu, R. Zhu, J. Zhu, X. Liang, G. Zhu, Y. Liu, Y. Xu, H. He, Fullerene modification of Ag3PO4 for the visible-light-driven degradation of acid red 18, RSC Adv. 6 (89) (2016) 85962–85969, https://doi.org/10.1039/C6RA18657B.
- [60] A.R. Silva, P.M. Martins, S. Teixeira, S.A.C. Carabineiro, K. Kuehn, G. Cuniberti, M. M. Alves, S. Lanceros-Mendez, L. Pereira, Ciprofloxacin wastewater treated by UVA photocatalysis: contribution of irradiated TiO2 and ZnO nanoparticles on the final toxicity as assessed by Vibrio fischeri, RSC Adv. 6 (98) (2016) 95494–95503, https://doi.org/10.1039/C6RA19202E.
- [61] X.-J. Wen, C.-G. Niu, L. Zhang, C. Liang, H. Guo, G.-M. Zeng, Photocatalytic degradation of ciprofloxacin by a novel Z-scheme CeO2–Ag/AgBr photocatalyst: Influencing factors, possible degradation pathways, and mechanism insight, J. Catal. 358 (2018) 141–154.
- [62] A.S. Giri, A.K. Golder, Ciprofloxacin degradation in photo-Fenton and photocatalytic processes: Degradation mechanisms and iron chelation, J. Environ. Sci. 80 (2019) 82–92.
- [63] M. Sarkhosh, M. Sadani, M. Abtahi, S.M. Mohseni, A. Sheikhmohammadi, H. Azarpira, A.A. Najafpoor, Z. Atafar, S. Rezaei, R. Alli, A. Bay, Enhancing photodegradation of ciprofloxacin using simultaneous usage of eaq—and OH over UV/ ZnO/I- process: Efficiency, kinetics, pathways, and mechanisms, J. Hazard. Mater. 377 (2019) 418–426.
- [64] Y. Picó, V. Andreu, Fluoroquinolones in soil—risks and challenges, Anal. Bioanal. Chem. 387 (4) (2007) 1287–1299, https://doi.org/10.1007/s00216-006-0843-1.
- [65] S. Guha, S. Saha, Fluoride Ion Sensing by an Anion $-\pi$  Interaction, Journal of the American Chemical Society 132(50) (2010) 17674-17677. h ttps://doi.org/10.1021/ja107382x.